THE JOURNAL OF PHYSICAL CHEMISTRY C
A JOURNAL OF THE AMERICAN CHEMICAL SOCIETY

pubs.acs.org/JPCC

Article

Effects of Self-Assembly on the Photogeneration of Radical Cations in Halogenated Triphenylamines

Muhammad Saddam Hossain, Ammon J. Sindt, Dustin W. Goodlett, Dylan J. Shields, Colin J. O'Connor, Aleksandra Antevska, Stavros G. Karakalos, Mark D. Smith, Sophya Garashchuk, Thanh D. Do, Anna D. Gudmundsdottir, and Linda S. Shimizu*

Cite This: *J. Phys. Chem. C* 2021, 125, 19991−20002

Read Online

ACCESS | Metrics & More | Article Recommendations | Supporting Information

ABSTRACT: We investigate the effect of assembly on charge transfer, charge recombination, and the persistence of radical cations in halogen-substituted triphenylamine (TPA) dimers. A series of urea-tethered TPA derivatives **1** (X = H, Cl, Br, and I) are compared, which have one phenyl group modified at the *para* position with a halogen. Ureas direct the assembly of these derivatives while halogen substituents influence the packing of the TPA units. These modifications affect the generation and persistence of TPA radical cations as monitored by electron paramagnetic resonance (EPR) spectroscopy. The formation and degradation pathways of the radical cations in solution and gas phase were probed by ion-mobility spectrometry mass spectrometry. In contrast, supramolecular assembly enhanced the stability of these materials as well as the persistence of their photogenerated radical cations, which appear to undergo charge recombination without degradation. Greater quantities of these radical cations are observed for the bromo and non-halogenated derivatives (**1Br**, **1H**). Time-dependent density functional theory (TD-DFT) calculations on single molecules and hydrogen-bonded dimers suggest the stability of TPA radical cations largely depends on initial photoinduced charge separation and electronic coupling between assembled TPA dimers. The latter was found to be about 7 times stronger in **1I** than in **1Br** dimers, which may explain faster charge recombination and shorter lifetimes of **1I** radicals. Transient absorption (TA) spectroscopy and TD-DFT were able to identify the charged species for **1Br** along with the kinetic traces and measured lifetime of ∼80 ns. Fluorescence quenching studies are consistent with initial charge separation and subsequent charge transfer event between nearby TPAs. Future exploration will focus on the mobility and application of these TPA assemblies as hole transport materials.

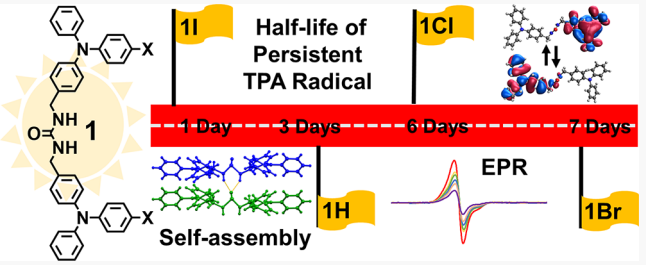

1. INTRODUCTION

Supramolecular assembly has proven to be an effective method for designing hierarchical materials.[1−3] Examples of self-assembled frameworks include supramolecular coordination cages,[4] covalent organic frameworks,[5] and hydrogen-bonded organic frameworks.[6,7] Precise organization of organic chromophores can afford new properties. For example, the assembly of perylene bis-imide dyes generates distinct optical properties[8] that can be further tailored for photoinduced energy and electron transfer.[9] The assembly of triphenylamines (TPAs) is of particular interest, as TPA and its derivatives form radical cations through chemical, electrochemical, or photoinduced oxidation.[10−12] These features make TPAs excellent hole transporters[13] and spin-containing magnetic materials.[14] Photoinduced processes allow TPAs to be used as a thin layer in optoelectronic devices such as perovskite-based solar cells,[15] organic solar cells,[16] organic light-emitting diodes (OLEDs),[17] and memory devices.[18] Amide-substituted triarylamines from Giuseppone's group form supramolecular polymers that show exceptional transport properties.[12,19] Yang's group found the hierarchical assembly of TPA-based metallocycles could be triggered by light, and the radical cations were significantly stabilized within these assemblies.[20]

In all these examples, the prerequisite for stable TPA radical cation formation is that all phenyl groups contain *para* substituents. Otherwise, upon radical generation the TPA rapidly dimerizes to form benzidines or other degradation products.[21,22] Even TPAs that are incorporated into macrocycles have their *para* positions carefully blocked.[23] Recent work suggests that supramolecular assembly has the potential to relax this constraint.[24,19,20] This may enhance spin−spin interactions and broaden the utility of TPA-based organic radicals.[25]

Received: June 4, 2021
Revised: August 11, 2021
Published: September 1, 2021

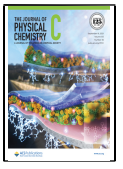

Downloaded via UNIV OF CINCINNATI on December 8, 2021 at 04:17:35 (UTC).
See https://pubs.acs.org/sharingguidelines for options on how to legitimately share published articles.

ACS Publications

© 2021 American Chemical Society

The Shimizu group employs urea directed self-assembly to organize dimers and macrocycles to afford robust and functional solid-state crystalline materials.[26,27] For example, UV-irradiation of unassembled TPA dimer **1Br** (Figure 1) in solution forms

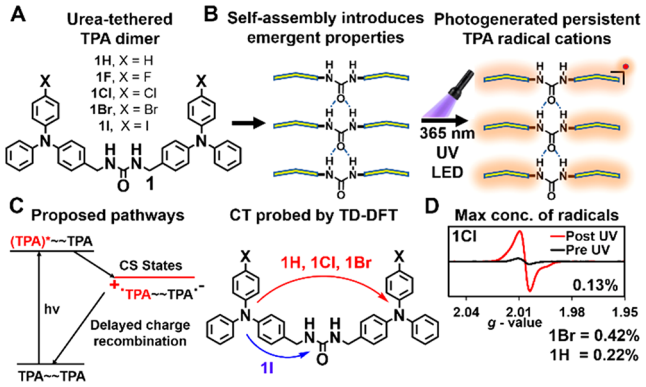

Figure 1. (A) The series of urea-tethered halogenated TPAs investigated. (B) Schematics of tape formation guided by urea hydrogen bonding. Irradiation of the assembled structures with 365 nm UV LEDs forms persistent TPA radical cations as monitored by EPR. (C) Proposed pathways to charge-separated (CS) states. TD-DFT calculations suggest charge transfer between the two urea tether TPA units for **1H**, **1Cl**, and **1Br** derivatives, while **1I** potentially undergoes charge transfer between the TPA and urea. (D) EPR spectra of **1Cl** and summary of maximum radical concentration compared with a calibration curve of magic blue: **1Cl** = 0.13% (red spectra after 16 h of irradiation), **1Br** = 0.42%, and **1H** = 0.22%.

radical cations that degrade in minutes; however, the assembled **1Br** affords photogenerated radical cations that appear to undergo the reverse electron transfer to return to the starting material without degradation.[24] The methylene urea-tethered dimers readily afford single crystals for X-ray diffraction, and radical formation in the crystals was monitored by electron paramagnetic resonance (EPR) spectroscopy. Electrochemical studies on **1Br** showed oxidation at 1.0 V versus a saturated calomel electrode (SCE). Bulk electrolysis at this potential gave a similar EPR spectrum as observed in the solid state, suggesting a radical cation was formed in both samples. Comparison of cyclic voltammograms of **1Br** and the controls indicates that the TPA unit undergoes reduction (−1.2 V vs SCE) before the methylene urea linker or halide.[28] We hypothesize that the initial photoinduced charge separation occurs by a transfer of an electron from one TPA unit to a neighboring TPA.

Here we synthesized urea-tethered TPA dimers **1F**, **1Cl**, and **1I** to complete the series and compared these structures with the previously reported **1Br** and **1H**. Halogens can influence the packing structures as well as modulate electronics by enhancing the probably of spin-forbidden transitions and increasing spin−orbit coupling.[29,30] These partial *para*-substituted compounds were anticipated to degrade in solution; however, we expected that assembly and crystallization would increase their stability. Ion-mobility spectrometry mass spectrometry was used to probe degradation processes and to examine if assembled structures could be detected. The photoinduced radical formation was followed by EPR to estimate the concentration and persistence of the radical cations. The stability of these materials before and after UV-irradiation was also probed by ^{1}H NMR, X-ray photoluminescence spectrometry (XPS), absorption, and emission studies. Laser flash photolysis (LFP) was performed on **1Br** to probe the initial photoinduced charged species. Time-dependent density functional theory (TD-DFT) calculations were used to analyze the frontier molecular orbitals and natural transition orbitals and to assess the charge transfer/separation and charge recombination on monomers and assembled dimers.

2. EXPERIMENTAL AND COMPUTATIONAL DETAILS

2.1. Characterization of Compounds. All commercially available reagents and solvents were purchased from VWR, Sigma-Aldrich, TCI America, and Alfa Aesar and were used without any further purification. Air-sensitive reagents were stored under nitrogen. Reactions were performed in oven-dried glassware covered with aluminum foil to protect from ambient light. ^{1}H NMR and ^{13}C NMR spectra were recorded in Bruker Avance 300 or 400 MHz spectrometers. Solvent peaks were used as a reference to report the chemical shift in ppm. High-resolution mass spectra were recorded in a direct exposure probe (DEP) in electron ionization (EI) mode on a Waters QTOF-I quadrupole time-of-flight mass spectrometer. Ion mobility mass spectrometry data of **1Br** were obtained by using an Agilent 6560 IMS-QTOF instrument.

2.2. X-ray Structure Determination. X-ray intensity data from a colorless needle were collected at 100(2) K by using a Bruker D8 QUEST diffractometer equipped with a PHOTON-100 CMOS area detector and an Incoatec microfocus source (Mo Kα radiation, λ = 0.71073 Å). The raw area detector data frames were reduced and corrected for absorption effects by using the Bruker APEX3, SAINT+, and SADABS programs.[31,32] The structure was solved with SHELXT.[33] Subsequent difference Fourier calculations and full-matrix least-squares refinement against F^2 were performed with SHELXL-2018[34] using OLEX2.[35]

2.3. Photophysical Properties and UV-Irradiation. Samples were dried under Ar(g) and loaded in EPR tubes, which were oriented horizontally and exposed to 365 nm waveform lighting real UV LED strips (4.5 W/ft, 3.2 ft). The photon flux was estimated as 9.78 × 10^{15} photons/s (see the Supporting Information). In solution, the absorption spectra were recorded in a Molecular Devices Spectramax M2. The diffuse reflectance of the solid sample was recorded by using a PerkinElmer Lambda 45 UV−vis spectrometer composed of UV Winlab software and was referenced to Spectralon. A PerkinElmer LS55 fluorescence spectrometer equipped with a pulsed high-energy source for excitation was used for emission analysis in solution, which was performed in a cuvette. Photoluminescence data in solid were collected on a HORIBA Scientific Standard Microscope Spectroscopy System connected with an iHR320 spectrometer and synchrony detector operating on Labspec 6 software. Spectra were recorded by using a 375 nm laser excitation source (power 0.3 mW) with 10× UV objective.

2.4. Laser Flash Photolysis (LFP) Measurements. Transient absorption measurements were performed by using a commercially available laser flash photolysis instrument (LP980, Edinburgh Instruments, Inc.) with laser excitation (266 nm, 6−7 mJ, 8 mm diameter, 3−5 ns FWHM, 10 Hz) provided by a pulsed neodymium-doped yttrium aluminum garnet (Nd:YAG) laser (Surelite II, Continuum, Inc.). The details of this setup have previously been described.[36] The data were converted to a text file in the L900 software and then plotted and analyzed in the IgorPro software. Solid-state nanocrystalline suspensions were prepared following the procedure reported previously.[37] Saturated acetone solutions of **1Br** were added to a water solution in a volumetric flask placed in an ultrasound bath until the absorption at 266 nm was

https://doi.org/10.1021/acs.jpcc.1c04933
J. Phys. Chem. C 2021, 125, 19991−20002

Table 1. Vertical Excitation Spectra and Types of Transitions, Energy, and Oscillator Strengths Assigned for Compounds 1H, 1Cl, 1Br, and 1I for the Three Strongest Transitions, Calculated with the CAM-B3LYP Functional Paired with 6-31+G or LANL2DZdp Basis Sets**

compound	level of theory	state	type	ΔE (eV)	f[a]	RMS electron−hole separation[b] (Å)	μ (D)[c]	|⟨r_e − r_h⟩|[d] (Å)
1H	CAM-B3LYP/6-31+G**	S_{10}	$\pi\pi^*$	4.160	0.030	4.055	1.399	0.163
		S_{14}	CT $\pi\pi^*$	4.382	0.412	4.131	4.983	1.273
		S_{16}	CT $\pi\pi^*$	4.413	0.179	4.108	3.274	1.008
1Cl	CAM-B3LYP/6-31+G**	S_6	$\pi\pi^*$	4.205	0.034	4.058	1.474	0.390
		S_8	CT $\pi\pi^*$	4.385	0.170	4.132	3.204	1.172
		S_9	CT $\pi\pi^*$	4.404	0.463	4.146	5.269	1.367
1Br	CAM-B3LYP/6-31+G**	S_6	$\pi\pi^*$	4.203	0.024	4.070	1.227	0.400
		S_9	CT $\pi\pi^*$	4.347	0.154	4.141	3.064	1.180
		S_{10}	CT $\pi\pi^*$	4.365	0.528	4.149	5.650	1.282
1I	CAM-B3LYP/LANL2DZdp	S_{14}	CT $\pi\pi^*$	4.175	0.088	4.250	2.358	1.434
		S_{19}	CT $\pi\pi^*$	4.360	0.129	4.212	2.799	1.280
		S_{20}	CT $\pi\pi^*$	4.384	0.186	4.245	3.352	1.627

[a]Oscillator strength. [b]Root-mean-square (RMS) electron−hole separation in angstroms. [c]μ magnitude of transition dipole moment (TDM) in debye. [d]Linear electron (e)/hole (h) distance in angstroms. The descriptor computed from transition density matrix and state character.

between 0.3 and 0.8. The resulting nanocrystalline suspension was placed inside a quartz cuvette with a 10 mm × 10 mm cross section and analyzed. The cuvettes were capped with a rubber septum and bubbled vigorously for 5 min with argon or oxygen to produce argon and oxygen-saturated conditions for appropriate analysis.

2.5. X-ray Photoelectron Spectroscopy (XPS) Analysis. XPS analysis was performed on a Kratos AXIS Ultra DLD XPS system with a monochromatic Al Kα source, operated at 15 keV and 150 W and pressures below 10^{-9} Torr. The X-rays were incident at an angle of 45° with respect to the surface normal. High-resolution core level spectra were measured with a pass energy of 40 eV, and analysis of the data was performed by using XPSPEAK41 software. The XPS system was equipped with a hemispherical electron analyzer and a load lock chamber for rapid introduction of samples without breaking vacuum. The XPS experiments were conducted by using an electron gun, directed on the sample for charge neutralization. The UV irradiation took place *in situ* through the windows of the ultrahigh-vacuum chamber.

2.6. Electron Paramagnetic Resonance (EPR) Measurements. EPR experiments were performed on a Bruker EMX plus equipped with a Bruker X-band microwave bridgehead and Xenon software (ver. 1.1b.66). The peak area was obtained by the double integration using Xenon software. Samples were sealed under argon and UV irradiated in Norell Suprasil quartz EPR tubes (diameter 3 mm).

2.7. Details of the Electronic Structure Calculations and Analysis. The electronic structure calculations were performed by using Q-Chem 5.3[38] and Spartan18 software.[39] Basis set exchange was used as a reference for selected bases.[40]

Because of practical considerations, the systems are modeled as single molecules in the gas phase. The geometry of the heavy atoms was taken from the SC-XRD data, while the positions of the hydrogen atoms were determined from the energy minimization in the gas phase employing the density functional theory (DFT) at the B3LYP-D3[41]/6-31G*[42] level. Theoretical UV−vis spectra and the excited state analysis are based on the time-dependent (TD) DFT calculations. Most results reported here (Tables S4−S7 and Table 1) are obtained with the CAM-B3LYP[43] functional paired with the 6-31+G** basis set. For the **1I** derivative, the iodine atom is represented by using the effective core potential basis LANL2DZdp.[44] CAM-B3LYP,[43] developed to improve the description of the charge-transfer excited states, is known to adequately describe the properties of dyes including the TPAs.[45] Additional TD-DFT calculations were performed by using LRC-ωPBEh[46] and B3LYP-D[41] functionals (same basis sets as above), and their results were found in qualitative agreement with those based on CAM-B3LYP.

Theoretical UV−vis spectra, $g(x)$, were generated as sums of Gaussian functions broadening the spectral lines.

$$g(x) = \sqrt{\frac{1}{\pi\sigma^2}} \sum_n f_n e^{-(x-x_n)^2/\sigma^2} \quad (1)$$

In eq 1, f_n and x_n represent the oscillator strength and the position of the nth line (in nanometers), respectively; x is the energy variable in nanometers. The width of the Gaussian is controlled by the standard deviation parameter σ set to 70, 20, 20, and 110 nm for **1H**, **1Cl**, **1Br**, and **1I**, respectively, to match the broad features of the experimental spectra.

The molecular orbitals (MOs)—the highest occupied/lowest unoccupied HOMO/LUMO—and the natural transition orbitals—the highest occupied/lowest unoccupied natural transition orbitals HONTO/LUNTO— were visualized with isovalue 0.04 in IQmol ver. 2.14.0. The spin at the nuclei was computed by using the Rassolov−Chipman operator for RC_{R0} = 0.25 au.[47]

2.8. Mass Spectrometry. The data were collected by using an Agilent 6560-IMS-QTOF mass spectrometer with the methods and instrument parameters previously reported.[48]

3. RESULTS AND DISCUSSION

3.1. Urea Directed Assembly of TPA. The **1H** and **1Br** urea tether TPA derivatives were prepared as described.[24,28] Three additional halogenated TPAs were synthesized by Ullmann condensation[49] followed by a Vilsmeier−Haack reaction (Scheme S1).[50] Reduction of the aldehyde[51] and treatment with phosphorus tribromide afforded the benzyl bromide,[52] which was coupled with triazinanone under basic conditions. Deprotection was performed in a mixture of 9:1 DMF/DEA (diethanolamine) at 90 °C under the acidic conditions to yield **1Cl**, **1I**, and **1F**. X-ray diffraction quality crystals were obtained by slow evaporation from acetonitrile solution for **1H**[28] and **1Cl** (10 mg mL^{-1}) or from ethyl acetate

https://doi.org/10.1021/acs.jpcc.1c04933
J. Phys. Chem. C 2021, 125, 19991−20002

solution for compound **1Br** (20 mg mL^{-1})[24] and **1I** (10 mg mL^{-1}), respectively. The geometries of the hydrogen bonds of **1H**, **1Cl**, **1Br**, and **1I** are summarized in Table S2. Thus far, attempts to crystallize **1F** by slow cooling, vapor diffusion, and slow evaporation have not yet yielded single crystals. We are currently screening a wider range of crystallization methods.

Crystals of **1I** were obtained as an ethyl acetate hemisolvate in the monoclinic space group $P2_1/c$. The asymmetric unit consists of one **1I** molecule and half of one ethyl acetate molecule, which is disordered about a crystallographic inversion center (Figure 2A). The conformation of **1I** is U-shaped with the two TPA units oriented in close proximity (Figure 2B). The intramolecular distance between the two TPA N centers d(N···N) is 9.9 Å. The urea adopts a *trans*−*trans* conformation and directs the assembly of infinite 1D H-bonded chains with d(N···O) distances of 2.887(5) and 2.891(5) Å and a twisting angle 36.28°. Figure 2C displays this assembly along the crystallographic *c*-axis. Additional, halogen bond type interactions are observed between iodine and urea carbonyl oxygen of a neighboring molecule with C−I···O distance of 3.305(1) Å, which is less than the sum of their van der Waals radii (3.50 Å).[53] Figure 2D displays the crystal packing of **1I**, which reveals ethyl acetate present in the interstitial space between the neighboring TPA units. The ethyl acetate is disordered but organized through halogen bonding with a carbonyl O atom−iodine C−I···O distance of 3.442(1) Å.

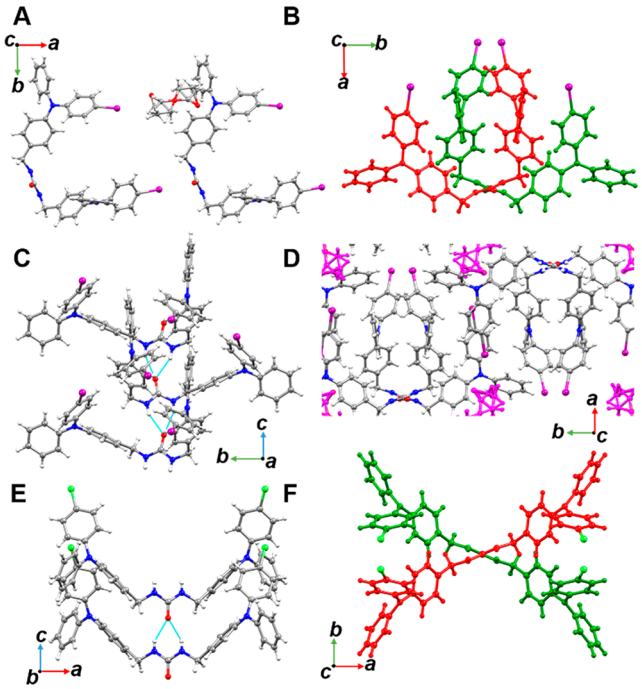

Figure 2. Comparison of urea-tethered halogenated TPAs **1I** and **1Cl**. (A) Hemisolvated crystal structure for **1I**. (B) Top-down view showing a U shape for **1I**. (C) Side view of urea−urea hydrogen-bonding interactions forming tapes of linked urea-tethered molecules of **1I**. (D) Packing of **1I** showing ethyl acetate solvent in the interstitial spaces between the neighboring TPAs. (E) View of linear urea hydrogen-bonding interactions in **1Cl**. (F) Top-down projection of the **1Cl** structure showing an X-shape.

In comparison, **1Br** crystallized in the orthorhombic system with the space group *Pccn*.[24] The two TPA units are stretched linearly outward from the urea groups in contrast to the U-shape of **1I**. The ureas are in a *trans*−*trans* conformation and organized into chains along the crystallographic *c*-axis (Figure S29A). The urea hydrogen bond distances are shorter (d(N···O) = 2.823(3) and 2.70(5) Å) with twisting angle of 51.6(1)° forming an X-shape in projection along the chain axis (Figure 29B). The **1Cl** is essentially isostructural to **1Br** (orthorhombic, *Pccn*). The urea hydrogen bond distances in **1Cl** are d(N···O) = 2.808(2) and 2.70(2) Å with a twisting angle of 47.74° (Figure 2E). Figure 2F shows the X-shape formed by the hydrogen-bonded chains of **1Cl** when viewed along the crystallographic *c*-axis.

The halide free **1H** crystallized in the orthorhombic system with centrosymmetric space group *Pbcn*.[28] Both TPA units extend opposite site of the disordered methylene ureas. The ureas adopt a *trans*−*trans* conformation with urea hydrogen bonding distances of d(N···O) = 2.749(8) and 2.716(8) Å and a twisting angle 16.32° (Figure S29C). These are the shortest H bonds and the smallest twisting angle observed in the series of compounds. Criss-crossing of urea-tethered chains forms a cruciform pattern projected along the crystallographic *c*-axis (Figure S29D, right).

Simulations from the Giuseppone group on triarylamine supramolecular polymers suggest that the relative orientation of neighboring TPA is important for the photophysical profile of TPA.[19] Analysis of our structures (Figures S68−S71) shows the packed TPA units of **1H**, **1Cl**, and **1Br** form similar snowflake conformations with N−N distances of 4.4 Å, supporting our comparison of these three compounds. **1I** in contrast gives a cross-flake conformation with a longer N−N distance of 13.7 Å. Further investigation of the propeller arrangement of the TPA phenyl rings within the same molecule suggests **1H**, **1Cl**, and **1Br** have a symmetrical orientation while **1I** shows a nonsymmetrical conformation (Figure S71).

Hirshfeld surface analysis was used to further analyze intermolecular interactions in the crystal structures of **1I**, **1Br**, and **1Cl**.[54] As expected, all show the key three centered urea−urea hydrogen bonding (Figures S31−32A); however, only **1I** has a significant halogen-bonding interaction. Figure 3A shows the intermolecular contact C−I···O 3.305 Å between the iodine and the carbonyl oxygen on a neighboring molecule, indicated in red. Additionally, there is a longer, weaker interaction between iodine with the oxygen atom of ethyl acetate solvent (3.442(1) Å) as compared with the sum of their van der Waals radii 3.50 Å.[53] The surface analysis also revealed C−I···π interaction (3.538 Å) between the TPAs for compound **1I** as seen in Figure S32D.

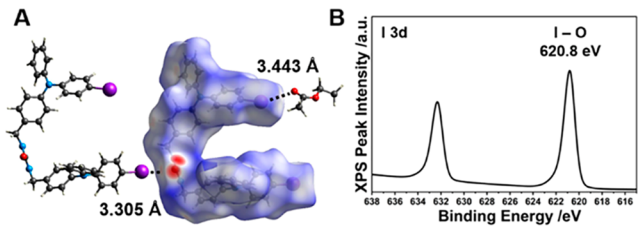

Figure 3. (A) Hirshfeld surface map for compound **1I** showing C−I···O interaction. (B) **I**(3d) XPS core level peaks for compound **1I** recorded with a monochromatic Al Kα X-ray source.

X-ray photoelectron spectroscopy (XPS) was used to probe the chemical environment around a halogen by examining the binding energy (BE) of the core level electrons. The detailed XPS spectra of the **1Cl**, **1Br**, and **1I** are shown in Figures S30 and Figure 3B. The core level peaks for **1Cl** (2p) 200.5 eV and **1Br**

https://doi.org/10.1021/acs.jpcc.1c04933
J. Phys. Chem. C 2021, 125, 19991−20002

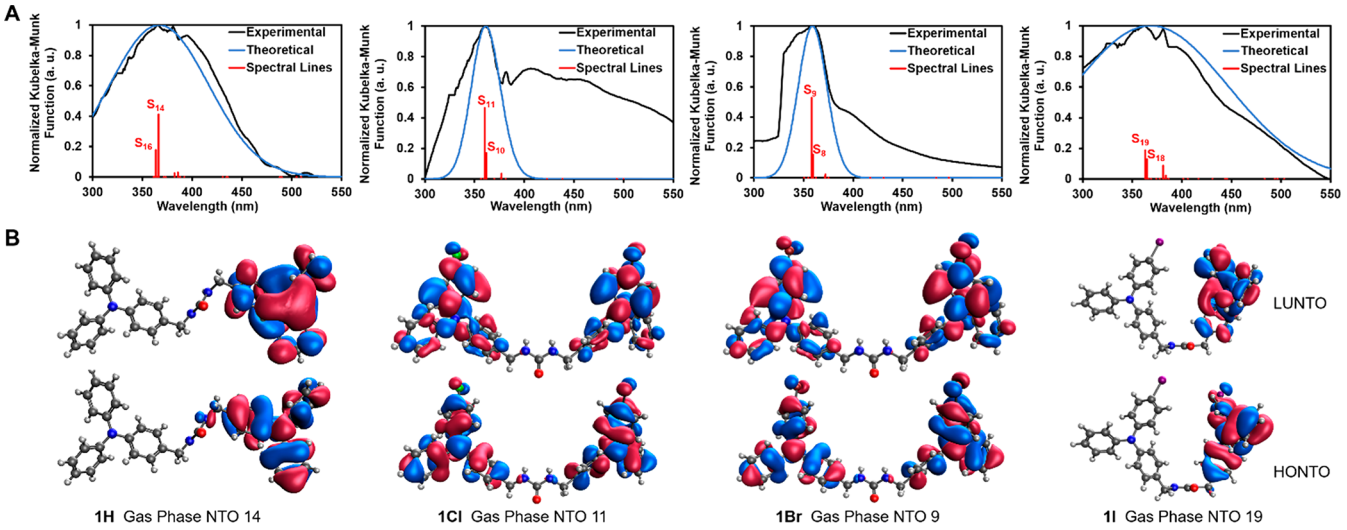

Figure 4. Comparison of normalized diffuse reflectance measurements of urea tethered TPAs (from left) **1H**, **1Cl**, **1Br**, and **1I** with TD-DFT calculated spectra including corresponding spectral lines. From left, transition to the S_{14} state corresponds to the λ_{max} of **1H** (366 nm), transition to the S_{11} state corresponds to the λ_{max} of **1Cl** (360 nm), transition to the S_9 state corresponds to the λ_{max} of **1Br** (358 nm), and transition to the S_{19} state corresponds to the λ_{max} of **1I** (363 nm). (B) Natural transition orbitals for urea-tethered TPAs (from left) **1H**, **1Cl**, **1Br**, and **1I** in the gas phase. HONTO (bottom); LUNTO (top).

(3d) 70.5 eV are characteristic of the reported literature values for C−Cl and C−Br bonds, respectively.[55,56] This suggests there are no significant halogen-bonding interactions in agreement with the XRD data. In contrast, the recorded BE core level peaks for **1I** display I(3d) core level peaks that are significantly different than typically observed 620.8 eV vs 619 eV.[57] Similar values for the I(3d) core level peaks (620.6 eV) were observed for C−I···O halogen bond formation between pyridyl bis-urea macrocycle and iodobenzene,[58] confirming the value of XPS for characterizing halogen-bonding interactions.

3.2. Absorption and Emission Spectra in Solution and Solid State. To investigate how the photophysics change with halide substitution, absorption and emission spectra were studied in argon-purged dichloromethane (DCM), ethyl acetate (EtOAc), and tetrahydrofuran (THF) solution (10 μM) as seen in Figures S33−S40. These studies are summarized in Table S3. All compounds displayed a similar absorption pattern ranging from 285 to 305 nm, which is attributed to strong $\pi-\pi^*$ transitions. For the emission spectra, the two bands arose with the first band around 360 nm and a second at ∼450 nm with the intensity of the second band increasing with more polar solvents. Upon assembly, all compounds displayed a sizable red-shift (55−66 nm). The twisting angle for **1H** was 16.32° with λ_{em} = 479 nm and a greater red-shift (113 nm). Derivatives with a larger twisting angle such as **1Br** (51.6°) exhibited a smaller red-shift (89 nm) and showed emission at a shorter wavelength, λ_{em} = 451 nm (Figure S41).

3.3. Simulations of Diffuse Reflectance by TD-DFT. The electronic structure calculations were performed for **1H**, **1Cl**, **1Br**, **1I** and the controls **2a** and **2b** as described in section 2.7. To assess the method dependence of the reported results, the excited states of **1Br** were also computed by using CAM-B3LYP[43]/LANL2DZdp,[44] LRC-ωPBEh[46]/6-31+G**,[42] and B3LYP-D3[42]/6-31+G**[43] methods, which qualitatively yielded similar results (Table S8). See the Supporting Information for further computational details.

The frontier molecular orbitals, their energies, and the HOMO−LUMO gap for the six molecules are presented for comparison in Figure S42. Both mono-TPA controls, **2a** and **2b**, show the characteristic electron distributions where the HOMO is primarily delocalized on the lone electron pair of nitrogen (N $2p_z$ orbital) throughout the phenyl rings. The LUMOs for **2a** and **2b** are localized or centered toward the nitrogen; there is no apparent contribution from the bromine or methylene urea. In comparison, in urea-tethered TPA dimer **1H**, the HOMO is localized in one unit of the TPA while the LUMO is localized in the other unit of the urea-tethered TPA. This is indicative of a charge-separated state, which is usually seen in donor−acceptor systems where TPA acts as a donor connected to an acceptor through the π-conjugated bridge.[59] The Cl- and Br-substituted dimers, **1Cl** and **1Br**, show their respective HOMO and LUMO delocalized through the whole molecule. In LUMO, one of the nitrogen centers lacks electron density, which can be attributed to the formation of the charge-transfer complex.

The iodo derivative **1I** exhibits a different trend. Here, the HOMO is localized on the urea-tethered TPA unit, while LUMO is localized on the phenyl ring partially substituted with iodine and methylene urea. This may be indicative of charge transfer between the TPA and methylene urea for **1I** instead of two TPA units in the other derivatives. The energy gaps of the controls and TPA dimers show modest variation ranging from 6.508 eV for **1I** to 6.821 eV for **1Cl**. Typically, the presence of electron-withdrawing groups such as Cl and Br increases the HOMO levels,[60] which was not observed within the dimer series as the HOMO of **1H** (−6.419 eV) is slightly higher than **1Cl** or **1Br** (−6.783 eV). We argue that within our set of four derivatives the structural effects of the halide substitutions play a significant role. We have used the **1Br** SC-XRD structure to generate two new theoretical structures in which the bromine atoms were replaced by H or iodine. While experimentally these structures could not be tested as crystal packing would alter the geometry, the computations are straightforward. These two structures are optimized (B3LYP-D3/6-31G*), allowing only hydrogens and the halides to move. Comparison of the HOMOs and NTOs at the strongest transitions (Figures S45 and S46) reveals that H and I incorporated into the "scaffold" geometry of **1Br** show comparable electronic transitions. Thus, packing

https://doi.org/10.1021/acs.jpcc.1c04933
J. Phys. Chem. C 2021, 125, 19991−20002

geometry is an important variable for controlling properties in these systems.

The UV−vis spectra have been constructed from the TD-DFT energies within the random phase approximation (RPA). Because the computed energy gaps in molecules or molecular clusters tend to be larger than those in solids (as seen for example in Table S9), the calculated excitation energies of **1H**, **1Cl**, **1Br**, and **1I** were multiplied by 0.773, 0.781, 0.793, and 0.779, respectively. These factors were determined by the best fit to the experimental data obtained for the crystalline samples. Once scaled, the shape of the computed absorption spectra is in good agreement with the experimental diffuse reflectance data.

For additional insight into the excited states, we have examined the natural transition orbitals (NTOs).[61] The highest occupied natural transition orbital (HONTO) and the lowest unoccupied natural transition orbital (LUNTO) were generated for the transitions of the highest oscillator strength. The frontier NTOs are presented in Figure 4 along with the experimental diffuse reflectance and the TD-DFT absorption spectra and spectral lines. The transitions closest to the maximum of experimental diffuse reflectance—their wavelength indicating λ_{max} given in parentheses—are S_{14} (366 nm), S_{11} (360 nm), S_9 (358 nm), and S_{19} (363 nm) for **1H**, **1Cl**, **1Br**, and **1I**, respectively. According to the spatial character of the corresponding NTOs, all four transitions are of $\pi\pi^*$ type. More specifically, while (i) similar to the frontier MOs the frontier NTOs of all four TPA derivatives lack electron density on their methylene urea moieties, (ii) in **1H** and **1I** these NTOs are localized only on one of the TPA units where the external unsubstituted phenyl ring has less electron density, and (iii) in **1Br** and **1Cl** they are delocalized over the entire molecular backbone.

The spin density (not shown) of **1H**, **1Cl**, **1Br**, and **1I** and the corresponding radical cations, probed by EPR, is consistent with the NTO trends above: the spin density of the radicals shows the same localization patterns as HOMO−1 of the neutral species (the spin density for the neutral species is essentially zero). Moreover, relevant to the EPR measurements, the spin on the nuclei is asymmetrically distributed between the TPA units in the cases of **1Cl** and **1Br** and is nearly equally split between the two units of **1H** and **1I**. The absolute values of the electron spins at the nuclei summed over the left/right TPA units are 0.000/0.333, 0.183/0.183, 0.177/0.187, and 0.445/0.000 for **1H**, **1Cl**, **1Br**, and **1I**, respectively. The maximum spin values are seen on the nitrogen atoms of the TPA centers; their values for the left/right TPA units in order of {**1H**, **1Cl**, **1Br**, and **1I**} are 0/0.099, 0.051/0.051, 0.049/0.052, and 0.126/0.000 (Table S12). Altogether, the analyses of the orbitals and spin density confirm the charge localization trend.

For more quantitative analysis of the charge transfer (CT) character in **1H**, **1Cl**, **1Br**, and **1I** upon UV−vis excitation, the RMS electron−hole separation,[62] the transition dipole moment (TDM) in debye (μ), and the linear electron−hole (e/h) distance in angstroms, encoded in the transition density matrix analysis,[63,64] are listed in Table 1 and Tables S4−S7 for the optically active transitions. The RMS e/h separations, which represent the exciton "size", characterize the dynamic charge separation. Electronic transitions associated with changes of the localized electron density and TDM are characterized by the transition type, which is either $\pi\pi^*$ or CT $\pi\pi$. The former describes a localized excitation ($\pi\pi^*$, small linear e/h separation); the latter describes the charge transfer state with the larger e/h separation.

These electron/hole descriptors were used to assign the transition type to the excited states. For **1H**, the states S_{14} and S_{16} with oscillator strength of 0.412 and 0.179 with RMS e/h distances of 4.131 and 4.108 show the highest change in TDM (4.983 and 3.274 D) and e/h separation (1.273 and 1.008 Å); these states are identified as CT $\pi\pi^*$ transitions. In contrast, the S_{10} state (TDM of 1.399 D and e/h separation of 0.163 Å) is assigned as $\pi\pi^*$. The rest of the states are similar to S_{10} and are identified as $\pi\pi^*$ transitions. Visualization of the NTOs further supports the argument as S_{14}, and S_{16} states show similar electron density distribution. For **1Cl**, **1Br**, and **1I** states (S_8, S_9), (S_9, S_{10}), and (S_{14}, S_{19}, S_{20}), respectively, are assigned as CT $\pi\pi^*$ transitions while the rest of the states are assigned as $\pi\pi^*$ transitions following similar trends as described earlier. On the basis of the NTO and transition density matrix analyses, we conclude that the urea-tethered TPA derivatives have CT characteristics at specific transition.

3.4. Mass Spectrometry. UV irradiation of compound **1Br** generates radicals that are persistent in the solid state; however, the molecule quickly degrades in solution.[24] We turned to ion-mobility spectrometry mass spectrometry to investigate the radical cation formation and its degradation products. The full ESI mass spectrum of **1Br** at 50 μM in 25:75 v/v ACN:H_2O with 0.1% FA (formic acid) and the ion mobility data of the monomeric species are shown in Figures 5A and 5B,

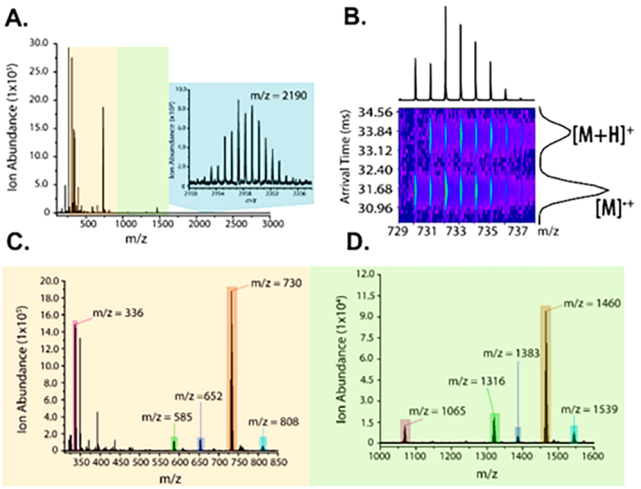

Figure 5. (A) Full ESI mass spectrum of **1Br** with the trimer in the inset. (B) 2D plot of m/z vs arrival time for the monomers, where the radical and protonated species can be distinguished based on monoisotopic masses. The isotopic peak distribution and arrival times indicate the existence of two distinct species. (C) Partial mass spectrum showing monomer (m/z = 730) and its fragments. (D) Partial mass spectrum containing the dimer (m/z = 1460) and radical-recombined by-products.

respectively. The solution was exposed to room light during the analysis process. Intact oligomers as large as the trimer (m/z 2190) were observed. The arrival time distribution in panel B reveals that there are two distinct monomeric species whose exact masses are consistent with a radical cation ($M^{\bullet+}$, m/z = 730) and protonated species ($[M + H]^+$, m/z = 731). Panels C and D highlight additional species detected in the low vs high mass region. Notably, m/z 336 is the most abundant fragment, which was identified as a Br-TPA radical cation (Figure S47A). Its isotope pattern is consistent with a Br-containing molecule (Br has two isotopes: ^{79}Br and ^{81}Br). Another interesting

https://doi.org/10.1021/acs.jpcc.1c04933
J. Phys. Chem. C 2021, 125, 19991−20002

fragment is m/z 585 (Figure S47B), corresponding to a radical cation degraded from a covalent dimer of **1Br**. This result is consistent with the fact that radical cations of **1Br** can degrade in minutes, and a minor population of covalent dimers may exist in solution. Interestingly, in the high mass region, we observed mass spectral peaks corresponding to the recombined by-products (m/z 1065, 1316, 1383, and 1539) of the radical cations (m/z 336, 585, 652, and 808) and **1Br**. For example, the Br-TPA fragment (m/z 335) combines with the **1Br** monomer (exact mass = 730 amu) to form a new species at m/z 1065. The byproducts are low abundance and color-coded in panels C and D based on their precursors. This result highlights the high propensity for the radical fragments to recombine with the abundant monomer. Finally, despite the radical fragments, the intact assembled oligomers (n = 2, 3) were still the dominant species during our experiments, indicating that assembled **1Br** is stable and can resist degradation.

3.5. EPR Experiments to Quantify Radical Generation.

In the solid state, no degradation of crystalline **1Br** was detected by SC-XRD, PXRD, and solution-state NMR even after 10 h of UV-irradiation using a Hanovia 450 W medium pressure Hg arc lamp.[24] Prior work showed lower intensity 365 nm LED's gives identical EPR spectra for **1Br** vs the mercury lamp, although longer irradiation time is required.[28] Some broadening of the aryl and carbonyl resonances was observed in the solid-state MAS ^{13}C NMR of **1Br**, which further indicated the delocalization of the electron density.[28] To examine the effect of the halogen heavy atom on the stability of the radicals, we turned to X-band EPR spectroscopy. Freshly recrystallized samples were filtered, dried under Ar (g) at room temperature, placed in quartz EPR tubes, and irradiated with 365 nm LEDs. The samples were then evaluated for radical generation, radical persistence, the maximum concentration of radicals, and lifetime at room temperature. The TPA dimer **1Br** (6.8 mg), and **1Cl** (10.5 mg) were triply recrystallized and showed good agreement between their EPR studies. The **1H** (8.1 mg) and **1I** (9.1 mg) samples were doubly recrystallized and showed good agreement. Figure 6 compares the EPR signals before and after UV irradiation on an incremental time scale for **1H**, **1Cl**, **1Br**, and **1I**. While pre-UV irradiation shows little to no EPR signal, post-UV irradiation dramatically increases the signal. **1H** and **1I** exhibit a broad, axial powder pattern shape EPR signal. **1Cl** and **1Br** show more anisotropy while retaining the powder pattern shape. The corresponding g-values for these urea tethered TPA derivatives are 2.006 (**1H**, **1Br**, **1I**) and 2.007 (**1Cl**), which are close to the g-value of TPA radical cations in solution (2.002−2.005).[65] This suggests that radical cations were formed in the supramolecular assembly.

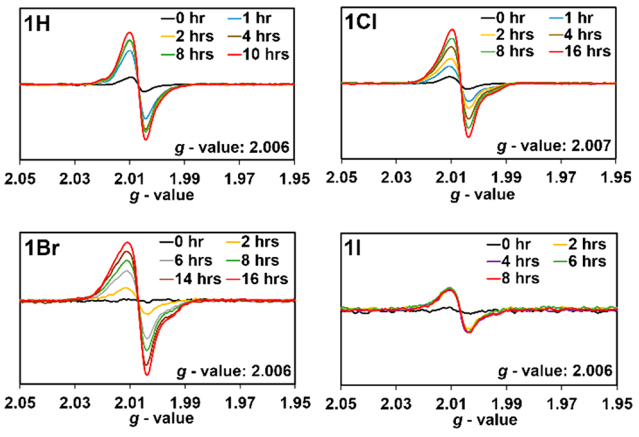

Figure 6. EPR studies of urea-tethered TPA derivatives at room temperature in the solid state. EPR signal pre- and post-UV irradiation (hours) of compound **1H**, **1Cl**, **1Br**, and **1I** with corresponding g-values.

To estimate the concentration of radicals generated, the double integration of the EPR spectra was plotted as a function of UV irradiation time (Figure S48). Next, the concentration of the radicals was approximated by comparing the data with a calibration of Magic Blue solutions in dry DCM (Figure S51). This comparison gives a qualitative estimate of radicals generated in the solid state. In each case, the percentage of radicals increased with longer irradiation time until reaching a plateau or maximum concentration, which can be seen in Figure 7. At these time points (~16 h (**1Cl**, **1Br**), ~10 h (**1H**), ~2 h

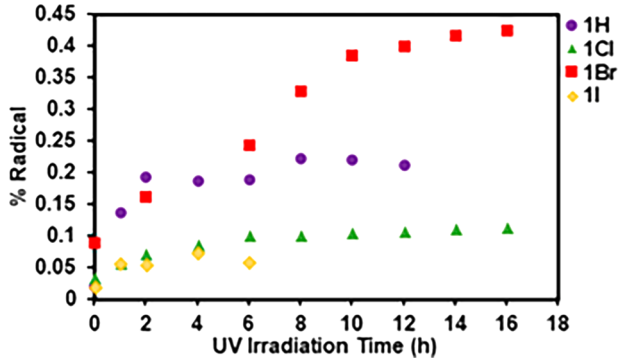

Figure 7. EPR studies of radical formation as a function of irradiation time for urea-tethered TPAs. Double integration of the EPR spectra over time of UV irradiation and later compared with the calibration curve of Magic Blue.

(**1I**)), we estimate the maximum concentration of radicals from the same number of radicals seen in 100 μL of a 0.30 mM (**1H**), 0.21 mM (**1Cl**), 0.20 mM (**1Br**), and 0.07 mM (**1I**) solution of Magic Blue. Accounting for the sample weight, the maximum concentrations of radicals followed the order of **1Br** > **1H** > **1Cl** > **1I** and ranged from a high of 0.42 ± 0.04% for **1Br** to very low, near our detection limit for **1I** (~0.06 ± 0.01%). We repeated the experiments two more times for both **1I** and **1Br** to estimate the error in these experiments as seen in Figures S48 and S50. The low radical concentration observed for **1I** could also be related to its solvate structure. Previously, we observed that host:guest complexes of TPA macrocycles with polar solvents exhibited lower radical concentrations.[28] Overall, parent **1H** and the chloro derivative **1Cl** showed similar percentages of radicals 0.22 ± 0.04% and 0.13 ± 0.04%, respectively. This was surprising as the heavy atom containing **1Cl** was expected to have a faster ISC rate in comparison to **1H**, which lacks a heavy atom.

Next, the persistence of photogenerated TPA radicals was probed by a dark-decay study. After being irradiated to their maximum radical concentrations, the samples were stored in the dark at room temperature under argon, and EPR spectra recorded over time. Figure 8A shows the EPR spectra recorded periodically for **1H** and **1Cl** (for **1I** see Figure S52). Again, the EPR signals were doubly integrated to obtain the area and plotted over time in Figure 8B. Fluctuations in the observed EPR signal intensity are likely due to the alignment of the crystals with respect to the applied field of the EPR instrument during

https://doi.org/10.1021/acs.jpcc.1c04933
J. Phys. Chem. C 2021, 125, 19991−20002

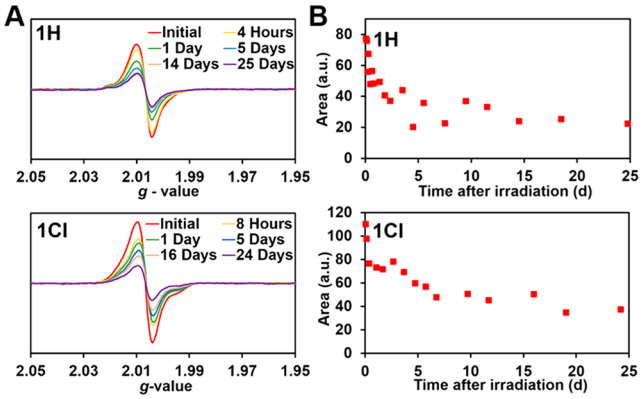

Figure 8. Dark decay EPR study of urea-tethered TPAs in the solid state after UV-irradiation to their maximum radical concentration. (A) EPR spectra generated after decay over time (left). (B) Double integration of the EPR spectra over time of UV irradiation (right).

measurements.[66,67] Half-lives were estimated by comparing the area at the maximum concentration of radicals until the area reaches half. As seen in Table 2, half-lives of the radicals were estimated ∼7 days for **1Br**,[24] ∼6 days for **1Cl**, and ∼3 days for **1H**.

Table 2. Analysis of Radical Generation Induced by UV-Irradiation

compound	max radical concentration (%)	half-lives (days)
1H	0.22	3
1Cl	0.13	6
1Br	0.42	7[a]
1I	0.06	<1

[a]Values taken from ref 10. A standard deviation of 0.04% and 0.01% was found for the average of three trials each for **1Br** and **1I**, respectively.

Previous studies on **1Br** showed that radicals can be observed even after 1 month and can be regenerated to re-exposure to light.[24] We continuously monitored the EPR signal for **1H** and **1Cl** to check the stability of these urea-tethered TPA derivatives. Even after 25 days (**1H**) and 24 days (**1Cl**) no change in the line shape of EPR spectra or corresponding *g*-value were observed, which demonstrates the stability of these derivatives and remarkable persistence of the TPA radical cation.

3.6. Transient Absorption Spectroscopy. LFP was used to identify charge-separated species formed during UV irradiation in the solid state. For the experiment, we prepared 1.4 μM nanocrystalline suspension of **1Br** in water in oxygen, air, and argon purged environments. Figure 9 shows the transient absorption (TA) spectra of nanocrystal suspension of **1Br** in degassed water (argon purged). The TA spectra of the **1Br** compound taken from 10−210 ns are broad with a peak around 650 nm (Figure 9A). The fact that the lifetimes were virtually unchanged in comparison to the error associated with kinetic measurements was unexpected as the triplet state should show lifetime quenching in the presence of oxygen. However, these crystalline materials are close-packed without pores, and triplet quenching would be expected to be primarily a surface phenomenon.[37] The rest of the wavelengths fit this general trend, and almost all lifetimes fell between 60 and 90 ns with monoexponential fits. According to the TD-DFT simulation of the TA absorption of **1Br**, the intense electronic transition at

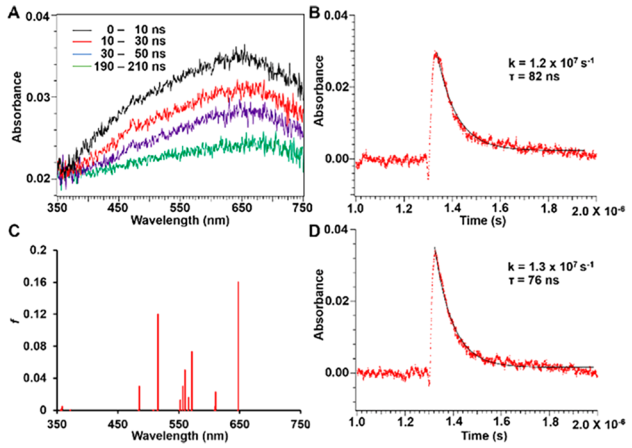

Figure 9. Transient absorption data, kinetic traces, and the TD-DFT spectral lines for **1Br** compounds. (A) Transient absorption spectra from 10−210 ns of argon degassed nanocrystalline suspensions in water upon 266 nm pulsed laser excitation. (B) Kinetic traces at 650 nm argon degassed nanocrystalline suspensions in water. (C) spectral lines from the TD-DFT calculation of the excited states at the LRC-ωPBEh/6-31+G** level. SC-XRD data were used for the calculation. (D) Kinetic traces at 650 nm oxygen degassed nanocrystalline.

around 650 nm (Figure 9C) is ascribed to the presence of a radical cation and in the range previously seen in solution.[68] The triplet transition is predicted to occur at 885 nm, which is outside the window for detection.

3.7. Solid-State Photoluminescence and Electronic Structure Analysis. A fluorescence quenching study was conducted to gain insight into the evolution of our systems after the initial formation of the charged species. The solid-state samples of the TPA derivatives were UV-irradiated for 6 h, and the fluorescence intensity (λ_{exc} = 375 nm) was compared pre-UV and post-UV irradiation. The same single crystal was used for both measurements. Upon UV irradiation (6 h), the fluorescence intensity of all these derivatives is reduced to about a quarter of the initial intensity (Figure S67). Because fluorescence quenching is expected after the initial formation of a CT complex,[69] these results suggest that the initial charge separation, facilitated by the organization and geometry of the TPAs, is followed by the rapid charge transfer between neighboring TPAs and, subsequently, by slower charge recombination. Slow recombination rate would be manifested in the unusual stability of the urea-tethered TPA radical cations in the solid state.

In support of the explanation above, we have focused on the particularly long-lived **1Br** radicals and examined the properties of the monomer and the hydrogen-bonded dimer and trimer, the latter two "stacked" to mimic their arrangement in a crystal according to the crystallographic data. Because of the extended system size (234 atoms for a trimer), the electronic structure calculations were performed by using a semiempirical method detailed in the Supporting Information; the results are summarized in Tables S9−S11. The hypothesis is that in solid-state UV-irradiation of the **1Br** samples leads to the intramolecular charge separation 2(TPA−TPA)* → (TPA−TPA)$^+$ + (TPA−TPA)$^-$, and the ions are long-lived due to small electronic coupling between the monomers in the ground state.

The computed energy differences of the charged monomers with respect to the ground state, E^0, and with respect to the UV−vis-populated excited state, E^*, of the neutral species

https://doi.org/10.1021/acs.jpcc.1c04933
J. Phys. Chem. C 2021, 125, 19991−20002

$\Delta = E^+ + E^- - 2E^0$ and $\Delta^* = E^+ + E^- - 2E^*$

show that the cation/anion pairs become energetically more stable for larger aggregates: Δ decreases from 674 to 557 kJ/mol while |Δ*| increases from 138 to 225 kJ/mol as we go from the isolated monomer to the trimer model. A more accurate DFT calculation for the monomer, yielding lower Δ and higher |Δ*| compared to the semiempirical results, suggests even larger stabilization of the charge-separated pairs due to the crystalline environment.

The electronic couplings in the ground state, related to the charge recombination, have been estimated by using Koopman's theorem as described in the Supporting Information (Table S10). As summarized in Table S10 for the **1Br** and **1I** dimers, the electron coupling in the **1I** model is about 7 times stronger than that for the **1Br** model, while the hole coupling is about 4 times stronger. This suggests that the charge recombination is more efficient in **1I** than in **1Br**, which is consistent with the longer radical lifetimes observed for **1Br**. Moreover, examination of the frontier orbitals (Figure S44) shows that the LUMO of **1Br** is delocalized over the two units, while the LUMO of **1I** is largely localized on one unit, which suggests that **1Br** is more likely to undergo intramolecular charge separation upon the UV−vis excitation compared to **1I**. This is consistent with the higher intensity of the radical generation in **1Br**. To summarize, (i) the intramolecular (intraunit) charge transfer upon UV irradiation is feasible, (ii) the charge recombination in the ground state is less likely for **1Br** than for **1I**, and (iii) a larger model size representing the solid state increases the stability of the charged (radical) pairs relative to the neutral pairs and reduces the excitation gap.

4. SUMMARY AND CONCLUSION

While introducing steric substituents on TPAs is a common method to stabilize radical cations in solution,[20,70] our work suggests self-assembly is a viable alternative strategy. The urea-tethered TPA dimers studied here lack typical electron acceptors and have unsubstituted *para* positions. As expected, these compounds form radical cations upon UV-irradiation in solution, which are not stable. Intriguingly, ion mobility spectrometry mass spectrometry also suggests that self-assembly stabilizes radicals. These MS studies on **1Br** were performed under exposure to light to detect radical degradation and recombination products produced from radical fragments recombining with the abundant monomers. Yet, assembled dimers and trimers were the dominant species, indicating that assembly is likely stabilizing even in the solution and gas phase.

Urea-guided assembly afforded single crystals for four of the structures, which enabled exploration of the effects of halogen substituents (heavy atoms) on photophysics and radical cation formation within a series of similar assembled structures. The structures of **1H**, **1Cl**, and **1Br** adopted antiparallel extended TPA conformations with an average TPA N···N distance of ∼14 Å. The N···N separation was slightly longer in **1H** (14.1 Å) as compared with ∼13.9 Å in **1Cl** and **1Br**. In contrast, **1I**, which alone crystallized as a solvate, adopts a U-shaped structure with a shorter N···N distance of 9.9 Å. **1I** exhibited both halogen- and hydrogen-bonding interactions.

In the solid state, the antiparallel extended TPA conformations of **1H**, **1Cl**, and **1Br** exhibited increased photogenerated radicals vs the U-shaped structure in the **1I** solvate. The **1Br** derivative displayed the highest efficiency of radical generation (maximum radical ∼0.42%) and longest lifetime/slowest recombination (half-life ∼7 days). Surprisingly, the **1H** derivative also generated large amounts of persistent TPA radical cations, despite lacking the heavy atom to facilitate spin−orbit coupling as well as containing four unsubstituted *para* positions that would typically speed degradation processes in solution. Analysis of frontier molecular orbitals indicates that two TPA groups tethered by methylene urea are necessary for the formation of a charge-separated state as compared with the untethered TPA.

Detailed TD-DFT studies were performed on monomers and assembled dimers of **1Br** and **1I** and for the **1Br** trimer. These studies suggest that UV-generated CT is feasible, favoring an intramolecular process for **1Br** vs **1I**. In addition, the electronic coupling leads to charge recombination roughly 7 times faster in **1I** as compared to **1Br**. Therefore, the observation that **1Br** displays both larger quantity and longer lifetime of radicals is reasonable as charge recombination in its ground state is less likely than in **1I**. Computations on larger models, that is, dimers and trimers used to represent assemblies and solid-state structures, show that although the neutral systems are energetically more favorable, the relative stability of the radical pairs increases with the size of the molecular model, providing support for the experimentally observed stabilization of radicals in the solid state. Currently, we are probing the rate of charge recombination and charge transport within both thin films and crystals of **1Br**, **1I**, and related derivatives to investigate if these charged radical pairs are mobile or if they represent unproductive, with respect to mobility, trapped states. A better understanding of how structure affects charge separation and mobility in assembled TPAs will promote the use of these materials as hole transporting layers for optoelectronic devices.

■ ASSOCIATED CONTENT

Supporting Information

The Supporting Information is available free of charge at https://pubs.acs.org/doi/10.1021/acs.jpcc.1c04933.

Synthetic procedures, product characterization, computational details, photophysical characterization, and EPR spectra (PDF)

Crystallographic data for **1Cl** (CIF)

Crystallographic data for **1I** (CIF)

■ AUTHOR INFORMATION

Corresponding Author

Linda S. Shimizu − *Department of Chemistry and Biochemistry, University of South Carolina, Columbia, South Carolina 29208, United States;* orcid.org/0000-0001-5599-4960; Email: shimizls@mailbox.sc.edu

Authors

Muhammad Saddam Hossain − *Department of Chemistry and Biochemistry, University of South Carolina, Columbia, South Carolina 29208, United States*

Ammon J. Sindt − *Department of Chemistry and Biochemistry, University of South Carolina, Columbia, South Carolina 29208, United States*

Dustin W. Goodlett − *Department of Chemistry and Biochemistry, University of South Carolina, Columbia, South Carolina 29208, United States*

Dylan J. Shields − *Department of Chemistry, University of Cincinnati, Cincinnati, Ohio 45221, United States*

Colin J. O'Connor − *Department of Chemistry and Biochemistry, University of South Carolina, Columbia, South Carolina 29208, United States*
Aleksandra Antevska − *Department of Chemistry, University of Tennessee, Knoxville, Tennessee 37996, United States;* orcid.org/0000-0003-2669-2853
Stavros G. Karakalos − *College of Engineering and Computing, University of South Carolina, Columbia, South Carolina 29208, United States;* orcid.org/0000-0002-3428-5433
Mark D. Smith − *Department of Chemistry and Biochemistry, University of South Carolina, Columbia, South Carolina 29208, United States*
Sophya Garashchuk − *Department of Chemistry and Biochemistry, University of South Carolina, Columbia, South Carolina 29208, United States;* orcid.org/0000-0003-2452-7379
Thanh D. Do − *Department of Chemistry, University of Tennessee, Knoxville, Tennessee 37996, United States;* orcid.org/0000-0002-1978-4365
Anna D. Gudmundsdottir − *Department of Chemistry, University of Cincinnati, Cincinnati, Ohio 45221, United States;* orcid.org/0000-0002-5420-4098

Complete contact information is available at: https://pubs.acs.org/10.1021/acs.jpcc.1c04933

Notes

The authors declare no competing financial interest.

■ ACKNOWLEDGMENTS

This work was supported in part by the National Science Foundation (CHE-1904386, CHE-1800140, and OIA-1655740). The computational work (S.G.) is based upon work supported in part by the NSF and by SCEPSCoR/Idea Program under Grants CHE-1955768 and OIA-1655740/20-GC02.

■ REFERENCES

(1) Stupp, S. I.; Palmer, L. C. Supramolecular Chemistry and Self-Assembly in Organic Materials Design. *Chem. Mater.* **2014**, *26*, 507−518.
(2) Lehn, J. M. Toward Complex Matter: Supramolecular Chemistry and Self-Organization. *Proc. Natl. Acad. Sci. U. S. A.* **2002**, *99*, 4763−4768.
(3) Adhikari, B.; Lin, X.; Yamauchi, M.; Ouchi, H.; Aratsu, K.; Yagai, S. Hydrogen-Bonded Rosettes Comprising π-Conjugated Systems as Building Blocks for Functional One-Dimensional Assemblies. *Chem. Commun.* **2017**, *53*, 9663−9683.
(4) Datta, S.; Saha, M. L.; Stang, P. J. Hierarchical Assemblies of Supramolecular Coordination Complexes. *Acc. Chem. Res.* **2018**, *51*, 2047−2063.
(5) Waller, P. J.; Gándara, F.; Yaghi, O. M. Chemistry of Covalent Organic Frameworks. *Acc. Chem. Res.* **2015**, *48*, 3053−3063.
(6) Luo, J.; Wang, J. W.; Zhang, J. H.; Lai, S.; Zhong, D. C. Hydrogen-Bonded Organic Frameworks: Design, Structures and Potential Applications. *CrystEngComm* **2018**, *20*, 5884−5898.
(7) Lin, R. B.; He, Y.; Li, P.; Wang, H.; Zhou, W.; Chen, B. Multifunctional Porous Hydrogen-Bonded Organic Framework Materials. *Chem. Soc. Rev.* **2019**, *48*, 1362−1389.
(8) Chen, Z.; Baumeister, U.; Tschierske, C.; Würthner, F. Effect of Core Twisting on Self-Assembly and Optical Properties of Perylene Bisimide Dyes in Solution and Columnar Liquid Crystalline Phases. *Chem. - Eur. J.* **2007**, *13*, 450−465.
(9) Würthner, F.; Saha-Möller, C. R.; Fimmel, B.; Ogi, S.; Leowanawat, P.; Schmidt, D. Perylene Bisimide Dye Assemblies as Archetype Functional Supramolecular Materials. *Chem. Rev.* **2016**, *116*, 962−1052.
(10) Quinton, C.; Alain-Rizzo, V.; Dumas-Verdes, C.; Miomandre, F.; Clavier, G.; Audebert, P. Redox-Controlled Fluorescence Modulation (Electrofluorochromism) in Triphenylamine Derivatives. *RSC Adv.* **2014**, *4*, 34332−34342.
(11) Saha, A.; Chen, M.; Lederer, M.; Kahnt, A.; Lu, X.; Guldi, D. M. Sulfur Rich Electron Donors-Formation of Singlet versus Triplet Radical Ion Pair States Featuring Different Lifetimes in the Same Conjugate. *Chem. Sci.* **2017**, *8*, 1360−1368.
(12) Moulin, E.; Armao, J. J.; Giuseppone, N. Triarylamine-Based Supramolecular Polymers: Structures, Dynamics, and Functions. *Acc. Chem. Res.* **2019**, *52*, 975−983.
(13) Agarwala, P.; Kabra, D. A Review on Triphenylamine (TPA) Based Organic Hole Transport Materials (HTMs) for Dye Sensitized Solar Cells (DSSCs) and Perovskite Solar Cells (PSCs): Evolution and Molecular Engineering. *J. Mater. Chem. A* **2017**, *5*, 1348−1373.
(14) Roquet, S.; Cravino, A.; Leriche, P.; Alévêque, O.; Frère, P.; Roncali, J. Triphenylamine-Thienylenevinylene Hybrid Systems with Internal Charge Transfer as Donor Materials for Heterojunction Solar Cells. *J. Am. Chem. Soc.* **2006**, *128*, 3459−3466.
(15) Petrus, M. L.; Schutt, K.; Sirtl, M. T.; Hutter, E. M.; Closs, A. C.; Ball, J. M.; Bijleveld, J. C.; Petrozza, A.; Bein, T.; Dingemans, T. J.; et al. New Generation Hole Transporting Materials for Perovskite Solar Cells: Amide-Based Small-Molecules with Nonconjugated Backbones. *Adv. Energy Mater.* **2018**, *8*, 1801605.
(16) Labrunie, A.; Gorenflot, J.; Babics, M.; Alévêque, O.; Dabos-Seignon, S.; Balawi, A. H.; Kan, Z.; Wohlfahrt, M.; Levillain, E.; Hudhomme, P.; et al. Triphenylamine-Based Push-Pull σ-C60 Dyad As Photoactive Molecular Material for Single-Component Organic Solar Cells: Synthesis, Characterizations, and Photophysical Properties. *Chem. Mater.* **2018**, *30*, 3474−3485.
(17) Zhao, J.; Yang, Z.; Chen, X.; Xie, Z.; Liu, T.; Chi, Z.; Yang, Z.; Zhang, Y.; Aldred, M. P.; Chi, Z. Efficient Triplet Harvesting in Fluorescence-TADF Hybrid Warm-White Organic Light-Emitting Diodes with a Fully Non-Doped Device Configuration. *J. Mater. Chem. C* **2018**, *6*, 4257−4264.
(18) Wu, J. H.; Liou, G. S. Substituent and Charge Transfer Effects on Memory Behavior of the Ambipolar Poly(Triphenylamine)S. *ACS Appl. Mater. Interfaces* **2015**, *7*, 15988−15994.
(19) Moulin, E.; Niess, F.; Maaloum, M.; Buhler, E.; Nyrkova, I.; Giuseppone, N. The Hierarchical Self-Assembly of Charge Nanocarriers: A Highly Cooperative Process Promoted by Visible Light. *Angew. Chem., Int. Ed.* **2010**, *49*, 6974−6978.
(20) Huo, G. F.; Shi, X.; Tu, Q.; Hu, Y. X.; Wu, G. Y.; Yin, G. Q.; Li, X.; Xu, L.; Ding, H. M.; Yang, H. B. Radical-Induced Hierarchical Self-Assembly Involving Supramolecular Coordination Complexes in Both Solution and Solid States. *J. Am. Chem. Soc.* **2019**, *141*, 16014−16023.
(21) Ito, A.; Ino, H.; Tanaka, K.; Kanemoto, K.; Kato, T. Facile Synthesis, Crystal Structures, and High-Spin Cationic States of All-*Para*-Brominated Oligo(N-Phenyl-m-Aniline)s. *J. Org. Chem.* **2002**, *67*, 491−498.
(22) Yano, M.; Sato, K.; Shiomi, D.; Ichimura, A.; Abe, K.; Takui, T.; Itoh, K. Synthesis of 1,3-Bis(Diarylamino)Benzenes as Model Precursors for One-Dimensional Organic Ferromagnetic Metals; Characterization of the Dications by Cyclic Voltammetry and Electron Spin Transient Nutation Spectroscopy. *Tetrahedron Lett.* **1996**, *37*, 9207−9210.
(23) Mao, L.; Zhou, M.; Shi, X.; Yang, H. B. Triphenylamine (TPA) Radical Cations and Related Macrocycles. *Chin. Chem. Lett.* **2021**.
(24) Sindt, A. J.; Dehaven, B. A.; McEachern, D. F.; Dissanayake, D. M. M. M.; Smith, M. D.; Vannucci, A. K.; Shimizu, L. S. UV-Irradiation of Self-Assembled Triphenylamines Affords Persistent and Regenerable Radicals. *Chem. Sci.* **2019**, *10*, 2670−2677.
(25) Miller, J. S. Magnetically Ordered Molecule-Based Materials. *Chem. Soc. Rev.* **2011**, *40*, 3266−3296.
(26) Shimizu, L. S.; Salpage, S. R.; Korous, A. A. Functional Materials from Self-Assembled Bis-Urea Macrocycles. *Acc. Chem. Res.* **2014**, *47*, 2116−2127.

(27) Dehaven, B. A.; Goodlett, D. W.; Sindt, A. J.; Noll, N.; De Vetta, M.; Smith, M. D.; Martin, C. R.; González, L.; Shimizu, L. S. Enhancing the Stability of Photogenerated Benzophenone Triplet Radical Pairs through Supramolecular Assembly. *J. Am. Chem. Soc.* **2018**, *140*, 13064−13070.
(28) Sindt, A. J.; DeHaven, B. A.; Goodlett, D. W.; Hartel, J. O.; Ayare, P. J.; Du, Y.; Smith, M. D.; Mehta, A. K.; Brugh, A. M.; Forbes, M. D. E.; et al. Guest Inclusion Modulates Concentration and Persistence of Photogenerated Radicals in Assembled Triphenylamine Macrocycles. *J. Am. Chem. Soc.* **2020**, *142*, 502−511.
(29) Turro, J. N.; Ramamurthy, V.; Scaiano, C. J. *Modern Molecular Photochemistry of Organic Molecules*; University Science Books: Sausalito, CA, 2010.
(30) Zhao, J.; Xu, K.; Yang, W.; Wang, Z.; Zhong, F. The Triplet Excited State of Bodipy: Formation, Modulation and Application. *Chem. Soc. Rev.* **2015**, *44*, 8904−8939.
(31) *APEX III, Version 2016.5-0 and SAINT+*, ver. 8.37A; Bruker AXS, Inc.: Madison, WI, 2016.
(32) Krause, L.; Herbst-Irmer, R.; Sheldrick, G. M.; Stalke, D. Comparison of Silver and Molybdenum Microfocus X-Ray Sources for Single-Crystal Structure Determination. *J. Appl. Crystallogr.* **2015**, *48*, 3−10.
(33) Sheldrick, G. M. SHELXT − Integrated Space-Group and Crystal-Structure Determination. *Acta Crystallogr., Sect. A: Found. Adv.* **2015**, *71*, 3−8.
(34) Sheldrick, G. M. Crystal Structure Refinement with SHELXL. *Acta Crystallogr., Sect. C: Struct. Chem.* **2015**, *71*, 3−8.
(35) Dolomanov, O. V.; Bourhis, L. J.; Gildea, R. J.; Howard, J. A. K.; Puschmann, H. OLEX2: A Complete Structure Solution, Refinement and Analysis Program. *J. Appl. Crystallogr.* **2009**, *42*, 339−341.
(36) Sarkar, S. K.; Upul Ranaweera, R. A. A.; Merugu, R.; Abdelaziz, N. M.; Robinson, J.; Day, H. A.; Krause, J. A.; Gudmundsdottir, A. D. Comparison of the Photochemistry of Acyclic and Cyclic 4-(4-Methoxy-Phenyl)-4-Oxo-but-2-Enoate Ester Derivatives. *J. Phys. Chem. A* **2020**, *124*, 7346−7354.
(37) Simoncelli, S.; Kuzmanich, G.; Gard, M. N.; Garcia-Garibay, M. A. Photochemical Reaction Mechanisms and Kinetics with Molecular Nanocrystals: Surface Quenching of Triplet Benzophenone Nanocrystals. *J. Phys. Org. Chem.* **2010**, *23*, 376−381.
(38) Shao, Y.; Gan, Z.; Epifanovsky, E.; Gilbert, A. T. B.; Wormit, M.; Kussmann, J.; Lange, A. W.; Behn, A.; Deng, J.; Feng, X.; et al. Advances in Molecular Quantum Chemistry Contained in the Q-Chem 4 Program Package. *Mol. Phys.* **2015**, *113*, 184−215.
(39) *Spartan'18*, ver. 1.4.4; Wavefunction, Inc.: Irvine, CA, 2019.
(40) Pritchard, B. P.; Altarawy, D.; Didier, B.; Gibson, T. D.; Windus, T. L. New Basis Set Exchange: An Open, Up-to-Date Resource for the Molecular Sciences Community. *J. Chem. Inf. Model.* **2019**, *59*, 4814−4820.
(41) Devlin, F. J.; Finley, J. W.; Stephens, P. J.; Frisch, M. J. Ab Initio Calculation of Vibrational Absorption and Circular Dichroism Spectra Using Density Functional Force Fields: A Comparison of Local, Nonlocal, and Hybrid Density Functionals. *J. Phys. Chem.* **1995**, *99*, 16883−16902.
(42) Ditchfield, R.; Hehre, W. J.; Pople, J. A. Self-Consistent Molecular-Orbital Methods. IX. An Extended Gaussian-Type Basis for Molecular-Orbital Studies of Organic Molecules. *J. Chem. Phys.* **1971**, *54*, 724−728.
(43) Yanai, T.; Tew, D. P.; Handy, N. C. A New Hybrid Exchange-Correlation Functional Using the Coulomb-Attenuating Method (CAM-B3LYP). *Chem. Phys. Lett.* **2004**, *393*, 51−57.
(44) Hay, P. J.; Wadt, W. R. Ab Initio Effective Core Potentials for Molecular Calculations. Potentials for the Transition Metal Atoms Sc to Hg. *J. Chem. Phys.* **1985**, *82*, 270−283.
(45) Bernini, C.; Zani, L.; Calamante, M.; Reginato, G.; Mordini, A.; Taddei, M.; Basosi, R.; Sinicropi, A. Excited State Geometries and Vertical Emission Energies of Solvated Dyes for DSSC: A PCM/TD-DFT Benchmark Study. *J. Chem. Theory Comput.* **2014**, *10*, 3925−3933.
(46) Rohrdanz, M. A.; Martins, K. M.; Herbert, J. M. A Long-Range-Corrected Density Functional That Performs Well for Both Ground-State Properties and Time-Dependent Density Functional Theory Excitation Energies, Including Charge-Transfer Excited States. *J. Chem. Phys.* **2009**, *130*, 054112.
(47) Rassolov, V. A.; Chipman, D. M. New Operators for Electronic Density Calculation. I. Derivations and Formal Analysis. *J. Chem. Phys.* **1996**, *105*, 1470.
(48) Link, B. A.; Sindt, A. J.; Shimizu, L. S.; Do, T. D. Selective Host-Guest Chemistry, Self-Assembly and Conformational Preferences of: M -Xylene Macrocycles Probed by Ion-Mobility Spectrometry Mass Spectrometry. *Phys. Chem. Chem. Phys.* **2020**, *22*, 9290−9300.
(49) Wang, L.; Shi, Y.; Zhao, Y.; Liu, H.; Li, X.; Bai, M. Push-Pull 1,8-Naphthalic Anhydride with Multiple Triphenylamine Groups as Electron Donor. *J. Mol. Struct.* **2014**, *1056−1057*, 339−346.
(50) Li, Z.; Dong, Q.; Xu, B.; Li, H.; Wen, S.; Pei, J.; Yao, S.; Lu, H.; Li, P.; Tian, W. New Amorphous Small Molecules - Synthesis, Characterization and Their Application in Bulk Heterojunction Solar Cells. *Sol. Energy Mater. Sol. Cells* **2011**, *95*, 2272−2280.
(51) Tian, H.; Yang, X.; Chen, R.; Zhang, R.; Hagfeldt, A.; Sun, L. Effect of Different Dye Baths and Dye-Structures on the Performance of Dye-Sensitized Solar Cells Based on Triphenylamine Dyes. *J. Phys. Chem. C* **2008**, *112*, 11023−11033.
(52) Dubinina, G. G.; Price, R. S.; Abboud, K. A.; Wicks, G.; Wnuk, P.; Stepanenko, Y.; Drobizhev, M.; Rebane, A.; Schanze, K. S. Phenylene Vinylene Platinum(II) Acetylides with Prodigious Two-Photon Absorption. *J. Am. Chem. Soc.* **2012**, *134*, 19346−19349.
(53) Bondi, A. Van Der Waals Volumes and Radii. *J. Phys. Chem.* **1964**, *68*, 441−451.
(54) Spackman, M. A.; Jayatilaka, D. Hirshfeld Surface Analysis. *CrystEngComm* **2009**, *11*, 19−32.
(55) Barthos, R.; Méhn, D.; Demortier, A.; Pierard, N.; Morciaux, Y.; Demortier, G.; Fonseca, A.; Nagy, J. B. Functionalization of Single-Walled Carbon Nanotubes by Using Alkyl-Halides. *Carbon* **2005**, *43*, 321−325.
(56) Ehlert, C.; Unger, W. E. S.; Saalfrank, P. C K-Edge NEXAFS Spectra of Graphene with Physical and Chemical Defects: A Study Based on Density Functional Theory. *Phys. Chem. Chem. Phys.* **2014**, *16*, 14083−14095.
(57) Moulder, J. F.; Stickle, W. F.; Sobol, P. E.; Bomben, K. D.; Chastain, J. *Handbook of X-Ray Photoelectron Spectroscopy*; Perkin-Elmer: Eden Prairie, MN, 1992.
(58) Som, B.; Salpage, S. R.; Son, J.; Gu, B.; Karakalos, S. G.; Smith, M. D.; Shimizu, L. S. Pillars of Assembled Pyridyl Bis-Urea Macrocycles: A Robust Synthon to Organize Diiodotetrafluorobenzenes. *CrystEngComm* **2017**, *19*, 484−491.
(59) Leliege, A.; Blanchard, P.; Rousseau, T.; Roncali, J. Triphenylamine/Tetracyanobutadiene-Based D-A-D π-Conjugated Systems as Molecular Donors for Organic Solar Cells. *Org. Lett.* **2011**, *13*, 3098−3101.
(60) Cias, P.; Slugovc, C.; Gescheidt, G. Hole Transport in Triphenylamine Based OLED Devices: From Theoretical Modeling to Properties Prediction. *J. Phys. Chem. A* **2011**, *115*, 14519−14525.
(61) Martin, R. L. Natural Transition Orbitals. *J. Chem. Phys.* **2003**, *118*, 4775−4777.
(62) Mewes, S. A.; Plasser, F.; Dreuw, A. Communication: Exciton Analysis in Time-Dependent Density Functional Theory: How Functionals Shape Excited-State Characters. *J. Chem. Phys.* **2015**, *143*, 171101.
(63) Plasser, F.; Wormit, M.; Dreuw, A. New Tools for the Systematic Analysis and Visualization of Electronic Excitations. I. Formalism. *J. Chem. Phys.* **2014**, *141*, 024106.
(64) Plasser, F.; Bäppler, S. A.; Wormit, M.; Dreuw, A. New Tools for the Systematic Analysis and Visualization of Electronic Excitations. II. Applications. *J. Chem. Phys.* **2014**, *141*, 024107.
(65) Forrester, A. R.; Hay, J. M.; Thompson, R. H. *Organic Chemistry of Stable Free Radicals*; Academic Press: New York, 1968.
(66) Žilić, D.; Rakvin, B.; Dalal, N. S. Study of the Local Field Distribution on a Single-Molecule Magnet by a Single Paramagnetic Crystal: A DPPH Crystal on the Surface of an Mn12-Acetate Crystal. *J. Appl. Phys.* **2011**, *110*, 093909.

https://doi.org/10.1021/acs.jpcc.1c04933
J. Phys. Chem. C 2021, 125, 19991−20002

(67) Yano, J.; Sauer, K.; Girerd, J.-J.; Yachandra, V. K. Single Crystal X- and Q-Band EPR Spectroscopy of a Binuclear Mn $_2$ (III, IV) Complex Relevant to the Oxygen-Evolving Complex of Photosystem II. *J. Am. Chem. Soc.* **2004**, *126*, 7486−7495.
(68) Pinzon, J. R.; Gasca, D. C.; Sankaranarayanan, S. G.; Bottari, G.; Torres, T.; Guldi, D. M.; Echegoyen, L. Photoinduced Charge Transfer and Electrochemical Properties of Triphenylamine Ih-Sc3N@C80 Donor-Acceptor Conjugates. *J. Am. Chem. Soc.* **2009**, *131*, 7727−7734.
(69) Doose, S.; Neuweiler, H.; Sauer, M. Fluorescence Quenching by Photoinduced Electron Transfer: A Reporter for Conformational Dynamics of Macromolecules. *ChemPhysChem* **2009**, *10*, 1389−1398.
(70) Schaub, T. A.; Mekelburg, T.; Dral, P. O.; Miehlich, M.; Hampel, F.; Meyer, K.; Kivala, M. A Spherically Shielded Triphenylamine and Its Persistent Radical Cation. *Chem. - Eur. J.* **2020**, *26*, 3264−3269.

https://doi.org/10.1021/acs.jpcc.1c04933
J. Phys. Chem. C 2021, 125, 19991−20002